Microelectronic Engineering 292 (2024) 112221

Contents lists available at ScienceDirect

Microelectronic Engineering

journal homepage: www.elsevier.com/locate/mee

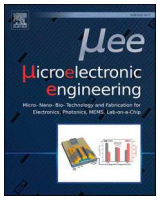

Chemical structure characteristics of flexible low-*k* SiCOH thin films etched by inductively coupled plasma-reactive ion etching process using FTIR and XPS spectra analysis

Thomas Poche [a,1], William Wirth [b,1], Seonhee Jang [a,*]

[a] Department of Mechanical Engineering, University of Louisiana at Lafayette, Lafayette, LA 70503, USA
[b] Fab Engineering, Samsung Austin Semiconductor, Austin, TX 78754, USA

ARTICLE INFO

Keywords:
Flexible low-k SiCOH
Chemical structure
Plasma-enhanced chemical vapor deposition
Inductively coupled plasma-reactive ion etching
Carbon fluoride

ABSTRACT

Flexible low dielectric constant (low-*k*) SiCOH thin films were fabricated onto flexible indium tin oxide coated polyethylene naphthalate (ITO/PEN) substrates using plasma-enhanced chemical vapor deposition (PECVD) of a tetrakis(trimethylsilyloxy)silane (TTMSS) precursor. RF plasma powers of 20 and 60 W were utilized for the deposition. The *k*-values of the pristine SiCOH films deposited at 20 and 60 W were 2.46 and 2.00, respectively. Both films showed hydrophobic surfaces. An inductively coupled plasma-reactive ion etching (ICP-RIE) process was then performed on the flexible SiCOH thin films using CF_4, $CF_4 + O_2$, and $CF_4 + Ar$. The surface wettability of the films increased substantially following etching, with many of the etched films being considered hydrophilic. The Fourier transform infrared (FTIR) spectra of the pristine films identified four prominent absorption bands as CH_x stretching, Si-CH_3 bending, Si-O-Si stretching, and Si-$(CH_3)_x$ stretching vibration modes. After the etching process, the peak area ratios of Si-O-Si stretching mode increased and those of Si-$(CH_3)_x$ stretching mode decreased. The X-ray photoelectron spectroscopy (XPS) spectra analysis determined significant concentration of fluorine on the surface of the film following etching. From the high-resolution XPS scan, it was found that the peak intensity of the C1s and Si2p peaks decreased after etching process and the peak center of the F1s peak shifted depending on etching chemistry. The *k*-values of the films at 20 W were fairly consistent while those of the films at 60 W increased significantly following the etching process. The increase in *k*-value after etching for the films at 60 W correlated with surface hydrophilicity, increase in the refractive index, and change in the peak area ratios of Si-O-Si and Si-$(CH_3)_x$ stretching modes in the FTIR spectra.

1. Introduction

Flexible electronics have been a subject of great interest within the microelectronics industries [1–3]. Unlike traditional electronics, which are developed onto a rigid Si wafer or other types of rigid substrates, flexible electronics are generally built upon a polymer substrate but also metal foil, paper, and flexible glass. Flexible electronic devices have an expanded range of applications due to their ability to fold, twist, stretch, or roll. Several applications of flexible electronics include flexible lighting and displays, wearable devices, and solar cells [4–13]. The flexible electronic devices may have additional requirements depending on its application. For example, flexible displays require a high degree of transparency. The development of flexible electronics involves a unique set of limitations relating to the substrate material. Polymers typically have a low glass transition temperature, so low temperature manufacturing methods must be employed to produce flexible electronic components. Various materials have been fabricated on flexible substrate using vacuum deposition techniques such as chemical vapor deposition, thermal evaporation, sputtering, and atomic layer deposition to fabricate flexible devices including solar cells, light emitting diodes, sensors, and transistors [14–20]. Although flexible electronics are fabricated with pattern transfer, solution printing process, roll-to-roll process, and additive manufacturing, they are not mature to apply for mass production yet [16,18,21,22]. Deposited functional materials could require photolithography and etching processes like traditional Si-based electronics.

* Corresponding author.
E-mail address: seonhee.jang@louisiana.edu (S. Jang).
[1] These authors contributed equally to this work

https://doi.org/10.1016/j.mee.2024.112221
Received 27 March 2024; Received in revised form 30 May 2024; Accepted 3 June 2024
Available online 4 June 2024

A wide variety of materials such as inorganic and organic molecules, semiconductors, dielectrics, and metals have been integrated for the fabrication of flexible electronic devices. One of the typical dielectric materials employed in semiconductor devices manufacturing is carbon-doped silicon oxide (SiCOH). The SiCOH is very important as a low dielectric constant (low-*k*, $k < 4.0$) layer in the interconnect or back-end-of-line (BEOL) process of semiconductor devices [23–34]. To utilize the SiCOH dielectric layer for flexible semiconductor devices, it should be patterned using the photolithography and etching processes. It has been reported that etching properties of the SiCOH thin films deposited on the rigid Si wafer are characterized under a dry etching process [35–46]. The SiCOH film typically consists of Si—O and hydrocarbon related bonding in the film structure. When it is exposed to plasma during the dry etching process, radicals, ion bombardment, and vacuum ultraviolet radiation cause damage to the material [35–39]. Etchants such as CF_4, O_2, and Ar in the dry etching process affect the structure and properties of the film. For example, CF_4 causes a fluorocarbon layer formed on the surface of the film [40–42]. Fluorine radicals in CF_4 plasma lead to the formation of Si-OH bonds on the surface, resulting in the film hydrophilic. The introduction of O_2 into the plasma can lessen polymerization upon the substrate surface and increase the concentration of fluorine atoms within the plasma [40]. O_2 plasma may damage the film through the removal of Si-CH_3 bonds and lead to undesired oxidation of the interconnects [34,43]. Introducing Ar into the plasma controls polymerization by the surface reactions through ion bombardment [44–46]. While the etching characteristics of the SiCOH dielectric films on the rigid Si substrate have been understood, little research has been performed regarding the etching characteristics of flexible SiCOH films. In this regard, an effect of etching parameters on material properties of flexible SiCOH dielectrics should be addressed to fabricate the flexible electronic devices.

In this study, flexible low-*k* SiCOH films were produced onto flexible indium tin oxide coated polyethylene naphthalate (ITO/PEN) substrates by plasma-enhanced chemical vapor deposition (PECVD) of a tetrakis (trimethylsilyloxy)silane (TTMSS, $C_{12}H_{36}O_4Si_5$) precursor at ambient temperature using a set of different plasma powers. The physical properties of the film including refractive index, extinction coefficient, surface morphology and roughness, and surface wettability were determined. In particular, the chemical bond structure and elemental composition of the flexible SiCOH films were analyzed by Fourier transform infrared (FTIR) spectroscopy and X-ray photoelectron spectroscopy (XPS). The *k*-values of the flexible SiCOH films were measured. An inductively coupled plasma-reactive ion etching (ICP-RIE) was performed to investigate the etching characteristics of the flexible SiCOH films under a set of carbon fluoride (CF_4)-based plasmas. Etching gas was selected among CF_4, $CF_4 + O_2$, and $CF_4 + Ar$. The physical, chemical, and electrical properties of the flexible SiCOH films were investigated to determine how the etching process affected the film.

2. Experimental details

2.1. Preparation of the flexible SiCOH films

Table 1 presents the deposition conditions of the SiCOH thin films which were deposited onto flexible ITO/PEN substates by the PECVD using the TTMSS ($C_{12}H_{36}O_4Si_5$, Sigma Aldrich, 97% purity). The ITO/PEN substrate was purchased from MTI corporation and had thicknesses of 180 nm and 125 μm on average for ITO and PEN, respectively. The PEN substrate was DuPont Teijin Teonex film-Q65HA. The ITO film was deposited by magnetron sputtering. It had a sheet resistance of 12 Ω/square and a transparency >75%. The ITO was covered by a protective film to prevent contamination, which was removed prior to loading in the PECVD reactor for deposition. The PEN sheets had a glass transition temperature of 120 °C, limiting the maximum allowable process temperature. Fig. 1(a) presents the molecular structure of the TTMSS precursor. The molecule is centered on a single Si atom bonded tetrahedrally to four O atoms. Each O atom is bonded to an outer Si atom, which is bonded to three methyl (CH_3) groups. The important bond structure to determine the SiCOH characteristics are the Si-O-Si at the center of the molecule and methyl functional groups branched off from each Si atom. A radio frequency (RF) power with 13.56 MHz was supplied to the PECVD system. Inside the PECVD reactor, a susceptor as a platform holding the substrate was placed at the bottom and a shower head including a precursor gas dispensing surface having multiple hole patterns was located at the top. The distance between the susceptor and the shower head was 20 mm. There was a bubbler containing the TTMSS precursor, equipped with an inlet and an outlet. The inlet of the bubbler was connected via a gas line and a regulator to the argon (Ar) gas cylinder containing Ar gas with a purity of 99.999% and the outlet via another gas line to the shower head. Ar gas was introduced into the heated bubbler through the inlet and vapors of the precursor were generated and delivered to the shower head through the outlet. Ar gas acted as a carrier gas to transfer the precursor vapors. The mixed flows with the precursor vapors carried by Ar gas flew into the reactor through the shower head. The flow of the precursor vapors was controlled by a mass flow controller (MFC) and a pressure flow controller (PFC). The MFC was installed between the Ar gas cylinder and the inlet of the bubbler and the PFC between the outlet of the bubbler and the reactor. A dry screw pump was located under the reactor via a vacuum line. After the substrate was loaded on the susceptor in the reactor, the pump started operating to lower the reactor pressure to 0.133 Pa, which was a base pressure prior to deposition. To vaporize the precursor effectively, the bubbler containing the TTMSS precursor was heated to 85 °C. The Ar flow rate flowing into the bubbler was maintained at 18 sccm via the MFC and the pressure flow of the vaporized precursor into the reactor at 30 Torr via the PFC. The SiCOH thin films were deposited at ambient temperature (18–19 °C) and a pressure of 26.7 Pa. The RF plasma power with 13.56 MHz was utilized with plasma powers of 20 and 60 W to examine films formed in two different plasma regimes. The reason to select two different plasma powers was because they contributed to different dielectric constants as well as chemical bonding configurations and film surface features which were strongly affected by etching process. Fig. 1(b) show a photo of the flexible SiCOH film deposited on ITO/PEN substrate along with a schematic of a cross-section of the SiCOH/ITO/PEN. The flexible SiCOH film was deposited on the ITO/PEN substrate without any delamination or cracks.

2.2. ICP-RIE process of the flexible SiCOH films

The flexible SiCOH films were then subjected to the ICP-RIE process. An Oxford ICP-DRIE System 100 ICP180 was utilized for the ICP-RIE process. A schematic diagram of the ICP-RIE process using CF_4 gas plasma can be seen in the **Supplementary Information (Fig. S1)**. Inside the process chamber, the SiCOH sample was situated in the bottom and electrically isolated from the rest of the chamber. Etching gas entered through the inlet in the top of the chamber and evacuated to the vacuum

Table 1
Deposition parameters for the SiCOH thin films using the PECVD process.

Plasma power (W)	Base pressure (Pa)	Temperature (°C)	Deposition time (min)	Deposition pressure (Pa)	Ar flow rate from MFC (sccm)	Pressure flow from PFC (Torr)
20	0.133	18–19	5	26.7	18	30
60	0.133	18–19	5	26.7	18	30

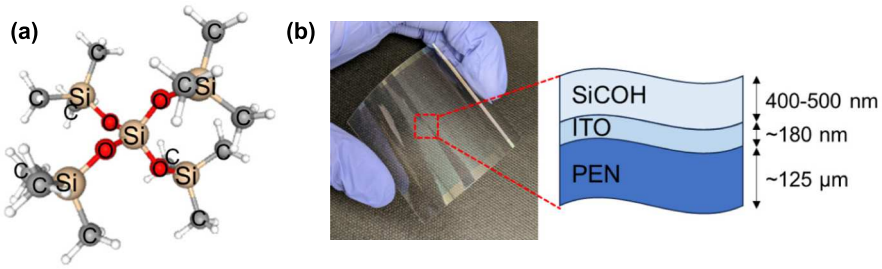

Fig. 1. (a) Molecular structure of the TTMSS precursor and (b) photo of flexible SiCOH film on ITO/PEN substrate along with a schematic of cross-section of SiCOH/ITO/PEN.

pump system through the outlet. The plasma was generated by an RF source which was supplied by inductively coupling the coils surrounding the ICP generation reactor. Generally, the ICP power controls the degree of ionization of the gas in the plasma and thus the plasma density. Separate RF and ICP generators offer separate control over ion energy and density. The ICP-RIE consists of chemical and physical mechanisms. The chemical mechanism is based on the reaction between radicals and the film surface to produce volatile by-products that are pumped out of the reactor. The physical mechanism is based on the high energy ion bombardment to the film surface, knocking out atoms or their agglomerates from the film. In plasma, reactive species such as ions, radicals, and electrons are found. Energetic electrons collide with a neutral etch gas molecules, creating reactions such as ionization, dissociation, dissociative ionization, excitation, attachment, dissociative attachment, and recombination. Positive ions are also important for etching process. Radicals are found more than ions in plasma. Radicals have a longer lifetime in plasma compared to ions because ions become neutralized during collisions with a surface while radicals often do not react with the surface and are back to plasma. The representative chemical reactions in plasma using CF_4, O_2, and Ar gases during ICP-RIE process can be seen in the **Supplementary Information (Table S1)**. Ionization, dissociation, dissociative ionization, excitation, attachment, and recombination are possible due to electron collisions. CF_4-based plasma generates active atoms, ions, fluorine radicals, and electrons that participate in both chemical and physical reactions with the film surface. By adding O_2 or Ar gases, more active species can contribute to the reactions in the plasma leading to acceleration or deceleration of etching process and affecting changes in the chemical structure of the film after etching.

Prior to etching of the flexible SiCOH films, O_2 plasma cleaning was performed on a bare Si wafer for 30 s to ensure a reproducible etching condition. The SiCOH thin films were then loaded into the ICP-RIE reactor and etched by the parameters outlined in Table 2. The etching gas was selected from CF_4, $CF_4 + O_2$, and $CF_4 + Ar$. The flow rate of CF_4 gas was maintained at 35 sccm, while the rates of O_2 and Ar gases were both maintained at 24 sccm. The RF plasma at 13.56 MHz was maintained at 200 W and the ICP power at 40 W. The operating pressure and temperature were 10.0 Pa and 25 °C, respectively. The length of each etching process was 30 s.

2.3. Characterization of the flexible SiCOH films

An ellipsometer (alpha-SE, J.A. Woollam) with a wavelength of 633 nm was used to measure the thickness, refractive index, and extinction coefficient of the pristine and etched SiCOH thin films. The etch rate of the film was calculated as the difference in film thickness before and after etching, divided by the etching time. An atomic force microscope (AFM, SmartSPM, Horiba) was utilized to measure the surface morphology and roughness of the films. A contact angle goniometer (L2004A, Oscilla) was utilized to measure the contact angle of the films. Elastic modulus and hardness were measured using nanoindentation (Nano Indenter G200, KLA) with continuous stiffness measurement (CSM) mode. The chemical structure of the flexible SiCOH films was analyzed using Fourier transform infrared (FTIR, Invenio-S, Bruker) spectroscopy and X-ray photoelectron spectroscopy (XPS, ESCA 2SR, ScientaOmicron). The FTIR instrument, which featured a Vari GATR attachment, scanned 64 times in the wavenumber range of 4000–600 cm^{-1} at a resolution of 4 cm^{-1}. The XPS machine featured a mono Al Kα X-ray source (1486.6 eV) at an emission angle of 90° and a circular analysis area 1.93 mm in diameter. The XPS survey scan range was 0–1200 eV at a scan resolution of 0.1 eV. The chamber pressure was held below 4×10^{-7} Pa, and a charge neutralizer was utilized during the analysis. High-resolution XPS scans were also performed across the Si2p, C1s, and F1s spectra ranges. A FDG 150 focused ion source was used to sputter the films using Ar ions at 4000 eV and a 45° incident angle. The XPS analysis was performed before and after the 2 min Ar ion sputtering to examine the changes in the elemental composition throughout the film. Constituent peaks in FTIR and XPS spectra were determined by the deconvolution using the Gaussian peak fitting from OriginPro and CasaXPS software, respectively. For the XPS peak fitting in the CasaXPS, the Shirley background method and the Gaussian-Lorentzian line shapes for peak fitting were utilized. The full width at half maximum (FWHM) and the peak position of each curve were unconstrained during fitting. A metal-insulator-metal (MIM, Al/SiCOH/ITO) structure was created to determine the C—V characteristics of the SiCOH film. For this purpose, aluminum (Al) dots were deposited onto the SiCOH thin films through electron beam evaporation. The Al dots had two areas of 0.005288 and 0.008093 cm^2 with a thickness of 120 nm. Capacitance-voltage curves of the MIM structure were measured using an LCR meter (J4287A, Agilent) at a frequency of 1 MHz. The dielectric constant (k) values were calculated from $C = \frac{k\varepsilon_0 A}{d}$, where C is the measured capacitance, k is the dielectric constant of the SiCOH film, ε_0 is the vacuum permittivity constant (8.854×10^{-12} F/m), A is the area of the Al electrodes, and d is the thickness of the SiCOH film.

Table 2
Parameters for plasma etching process using ICP-RIE.

Etching conditions	Operating pressure (Pa)	Temperature (°C)	RF power (W)	ICP power (W)	Etching time (s)	CF_4 flow rate (sccm)	O_2 flow rate (sccm)	Ar flow rate (sccm)
CF_4	10.0	25	200	40	30	35	0	0
$CF_4 + O_2$	10.0	25	200	40	30	35	24	0
CF_4 + Ar	10.0	25	200	40	30	35	0	24

3. Results and discussion

3.1. Properties of pristine flexible SiCOH thin films

Table 3 displays the material properties of the pristine flexible SiCOH films on ITO/PEN substrates for deposition plasma powers of 20 and 60 W. The average *k*-values were 2.46 and 2.00 for the films at 20 and 60 W, respectively. The film deposited at 60 W had a lower *k*-value than the film at 20 W. The contact angles for the films at 20 and 60 W were measured to be 107.61 and 106.97°, respectively. A hydrophobic material is defined as having a contact angle >90°, thus both films were hydrophobic in nature. The surface roughness was calculated using the root mean square (RMS) across the heights and depths of the surface. The RMS values were 0.290 and 1.070 nm for the films at 20 and 60 W, respectively. The films deposited at 60 W exhibited an increased roughness compared to the films at 20 W. The refractive indices were 1.444 and 1.473 for the films at 20 and 60 W, respectively. It is known that refractive index has a positive correlation with film density, which generally indicates higher mechanical strength. The extinction coefficients were 0.00049 and 0.00003 for the films at 20 and 60 W, respectively. Materials with an extinction coefficient below 0.01 are widely considered to be transparent [47]. The elastic modulus and hardness values of the film at 60 W were 8.325 and 1.229 GPa, respectively, which were higher than the values for the film at 20 W. This indicates a correlation between increased film density and increased mechanical strength. Two flexible SiCOH films fabricated at different plasma powers showing different material properties were utilized to address etching characteristics.

3.2. Physical properties of etched flexible SiCOH thin films

Table 4 presents physical properties of etched flexible SiCOH thin films deposited at 20 and 60 W for etching with CF_4, $CF_4 + O_2$, and $CF_4 + Ar$ plasma. Fluorine-based plasma etching is required to etch the SiCOH films because silicon can be removed from the film through the formation of volatile SiF_x compounds from the reaction between silicon and fluorine [47,48]. In addition, carbon is removed from the film through the creation of volatile fluorocarbons from the reaction between carbon and fluorine. Ion bombardments during etching process contribute to breaking the Si—O and Si—C bonds of the film. Compared to CF_4 and $CF_4 + O_2$, the etching rate was reduced for the films etched under $CF_4 + Ar$ gas for both 20 and 60 W. The addition of Ar gas into the reaction chamber is known to reduce the concentration of fluorine within the fluorocarbon layer that forms on the substrate surface during the etching process [41]. This change in fluorine concentration results in fewer SiF_x compounds being formed, reducing the etch rate. Etch rates for $CF_4 + O_2$ were relatively higher with 3.89 and 3.52 nm/s for 20 and 60 W, respectively. This can be explained by oxygen's interaction with CF_x radicals which contributes to an increase in CF_4 dissociation causing more CF_x radical concentration [49,50]. It was known that the etch rate can considerably increase by additional oxygen and oxygen radicals may damage the low-*k* films especially if they are porous [51]. Reactive oxygen atoms diffused into the film break Si-CH_3 bonds and form hydrophilic Si-OH bonds [52,53].

The refractive index of the flexible SiCOH films before and after the etching process was measured. It is known that refractive index has a positive correlation with the density of the material [54,55]. The refractive index of the films at 20 W remained largely unchanged regardless of etching condition and slightly increased from 1.444 to 1.450 after etching under $CF_4 + O_2$. The refractive index of the films at 60 W was affected more significantly by the etching processes, increasing from 1.473 regardless of the composition of the etching plasma. The film etched under CF_4 etching gas exhibited the largest refractive index of 1.524, followed by 1.513 and 1.496 for the films etched under $CF_4 + O_2$ and $CF_4 + Ar$, respectively. An increase in refractive index is expected to be correlated with less porosity, i.e., densification of the film causing a higher *k*-value [56,57]. It is possible that the SiCOH films at 60 W could bring increased *k*-values after etching process based on the increased refractive index. The extinction coefficient of the flexible SiCOH films before and after the etching process was also measured. Low extinction coefficient values are important for several flexible device applications, such as flexible displays. It was generally accepted that materials having the extinction coefficient below 0.01 are transparent [47]. The pristine and etched films all showed extinction coefficient values substantially lower than 0.01, ranging from 0.00049 to 0.00003, confirming the films to be transparent in nature. The extinction coefficient was hardly affected by the etching process, retaining transparency.

Fig. 2(a)-(d) presents the AFM surface morphology of the pristine and etched flexible SiCOH thin films with CF_4, $CF_4 + O_4$, and $CF_4 + Ar$ plasma, respectively. The deposition plasma power was 20 W. Each scan was performed over a 1 μm × 1 μm area of the SiCOH films. The difference between the highest and lowest points of the scanned areas is shown by the vertical scale bars on the right of each image. The height range of the pristine film was 3.1 nm. The films etched under CF_4 and $CF_4 + O_2$ plasma had increased height ranges of 4.6 and 3.5 nm, respectively, while the film etched under $CF_4 + Ar$ had a decreased height range of 2.5 nm. Fig. 3(a)-(d) shows the AFM surface morphology of the pristine and etched flexible SiCOH thin films with CF_4, $CF_4 + O_2$, and $CF_4 + Ar$ plasma, respectively, when the deposition plasma power was 60 W. The height range of the pristine film was 8.6 nm. The film etched under CF_4 had a slightly increased height range of 8.7 nm, while the films etched under $CF_4 + O_2$ and $CF_4 + Ar$ had decreased height ranges of 2.2 and 6.1 nm, respectively. It was observed that overall morphology of the films after etching in $CF_4 + O_2$ showed smoother than those in CF_4 and $CF_4 + Ar$ for both 20 and 60 W.

The RMS roughness values were calculated from the AFM surface topography scans of the pristine and etched flexible SiCOH thin films. It is known that etch chemistry has an effect on surface roughness, and that surface roughness and film porosity have a positive correlation [58]. The surface roughness values were all below 1.1 nm, which is quite low compared to the measured film thickness of 400 to 500 nm. The roughness of the pristine film at 20 W was 0.290 nm, which increased to 0.513 and 0.451 nm after etching under CF_4 and $CF_4 + Ar$ plasma, respectively. A slight reduction of roughness to 0.241 nm was observed following etching under $CF_4 + O_2$. The roughness of the pristine film at 60 W was 1.070 nm, which decreased to 0.916, 0.229, and 0.747 nm for the films etched under CF_4, $CF_4 + O_2$, and $CF_4 + Ar$, respectively. The flexible SiCOH thin films etched under $CF_4 + O_2$ showed the lowest roughness values for the films deposited at both plasma powers. This was consistent with the surface morphology images, showing smoother surfaces for $CF_4 + O_2$.

The contact angle values were obtained for the pristine and etched flexible SiCOH thin films to observe the surface wettability. A material

Table 3
Material properties of pristine flexible SiCOH thin films.

Plasma power (W)	Dielectric constant (*k*)	Contact angle (degree)	RMS roughness (nm)	Refractive index (*n*)	Extinction coefficient (*k*)	Elastic modulus (GPa)	Hardness (GPa)
20	2.46	107.61	0.290	1.444	0.00049	1.418	0.042
60	2.00	106.97	1.070	1.473	0.00003	8.325	1.229

Table 4
Physical properties of etched flexible SiCOH thin films.

Deposition plasma power (W)	Etching condition	Etch rate (nm/s)	Refractive index	Extinction coefficient	RMS roughness (nm)	Contact angle (degree)
20	Pristine	–	1.444	0.00049	0.290	107.61
	CF_4	2.74	1.448	0.00039	0.513	93.98
	$CF_4 + O_2$	3.89	1.450	0.00031	0.241	63.40
	$CF_4 + Ar$	0.41	1.449	0.00034	0.451	70.88
60	Pristine	–	1.473	0.00003	1.070	106.97
	CF_4	4.09	1.524	0.00020	0.916	73.57
	$CF_4 + O_2$	3.52	1.513	0.00036	0.229	22.14
	$CF_4 + Ar$	1.58	1.496	0.00017	0.747	64.55

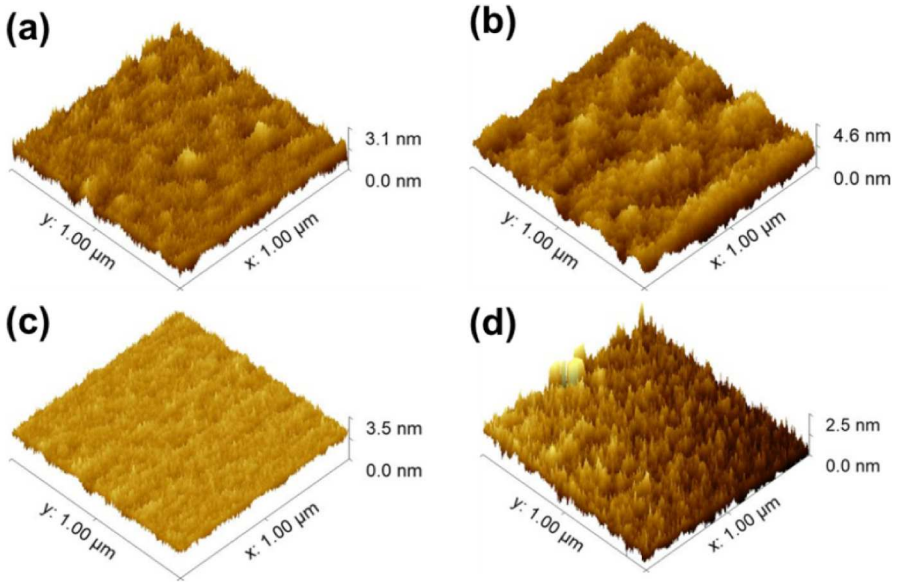

Fig. 2. AFM surface morphology of (a) pristine and etched flexible SiCOH thin films using etching gases of (b) CF_4, (c) $CF_4 + O_2$, and (d) $CF_4 + Ar$ for the deposition plasma power of 20 W.

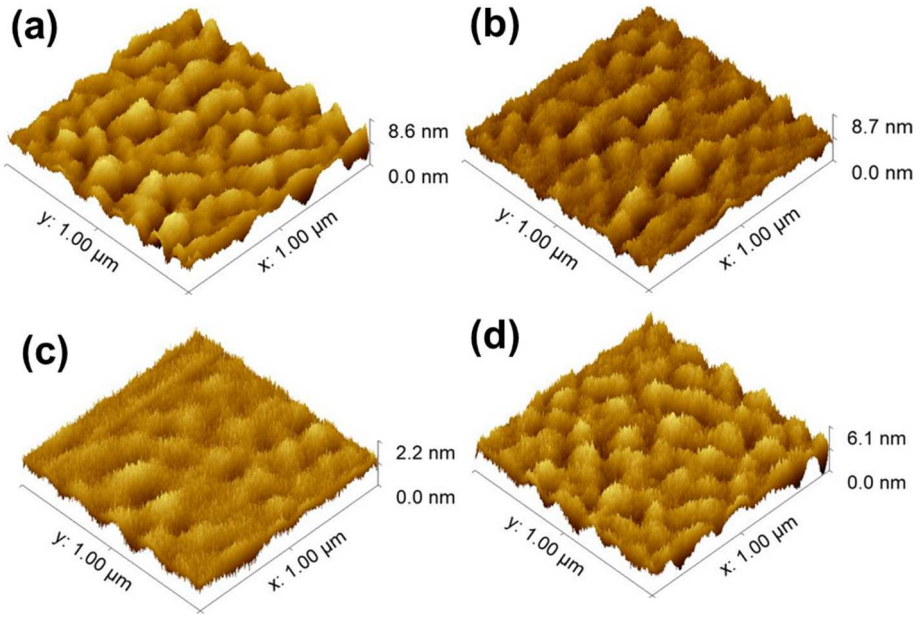

Fig. 3. AFM surface morphology of (a) pristine and etched flexible SiCOH thin films using etching gases of (b) CF_4, (c) $CF_4 + O_2$, and (d) $CF_4 + Ar$ for the deposition plasma power of 60 W.

with a contact angle above 90° is considered hydrophobic, while a contact angle below 90° suggests that the material is hydrophilic. The contact angle values for the pristine SiCOH films were found to be 107.61° and 106.97° for the films at 20 and 60 W, respectively, which indicated both the pristine films were hydrophobic. The contact angle of the flexible SiCOH films decreased significantly following the etching process due to plasma damage. All but one of the etched films had a contact angle values <90°, marking them as hydrophilic. The hydrophilic surface is associated with a reduction in methyl groups due to the reaction between the film surface and plasma during the etching process [59]. It was known that the SiCOH films become hydrophilic due to plasma damage and have an increased dielectric constant when water adsorption easily occurs on the film surface [59]. The film deposited at 20 W after etching in CF_4 had a contact angle of 93.98°, meaning that it was slightly hydrophobic. The largest drop in contact angles of 63.40 and 22.14° were observed after etching in $CF_4 + O_2$ for the films at 20 and 60 W, respectively. The most hydrophilic surface was obtained by adding O_2 to CF_4 plasma for both 20 and 60 W. It is likely that the etching in $CF_4 + O_2$ induced smoother and more hydrophilic surface. Overall, the flexible SiCOH thin films became more hydrophilic as a result of additional etchant such as Ar or O_2 to CF_4 plasma during the etching process.

3.3. FTIR analysis

The chemical composition of the flexible SiCOH films before and after etching was determined using FTIR analysis. Fig. 4(a) and (b) presents the FTIR spectra of the pristine and etched flexible SiCOH films deposited at plasma powers of 20 and 60 W, respectively, in the wavenumbers of 1500–650 cm^{-1}. Three prominent peaks in the FTIR spectra were associated with Si-O-Si stretching, Si-CH_3 bending, and Si-$(CH_3)_x$ stretching modes at the wavenumbers of 1200–900, 1300–1200, and 950–650 cm^{-1}, respectively [58]. Additionally, CH_x stretching mode was found at 3100–2800 cm^{-1}. The CH_x stretching peak was not shown due to its relatively lower peak intensity than the other three peaks. Both deposition plasma power and etch chemistry influenced the chemical bond structure of the flexible SiCOH films. For the pristine SiCOH films, overall peak intensities increased as the plasma power increased from 20 to 60 W. The intensity of the Si-CH_3 bending peak increased greatly following etching for both plasma powers. The films at 20 W displayed a comparatively narrow Si-O-Si stretching mode with a higher peak intensity while the films at 60 W showed a broader Si-O-Si stretching mode without much change in its peak intensity after the etching process. The Si-$(CH_3)_x$ stretching mode changed its peak shape varying its constituent peaks after the etching process. Fig. 4(c) shows the peak area ratio for the four major peaks in the FTIR spectra for the films deposited at 20 and 60 W before and after the etching process. The peak area ratio values were calculated by dividing the peak area of the peak in question by the total peak area of all four peaks. The Si-O-Si stretching mode was dominant for all SiCOH films both before and after etching. For the films at 20 W, the peak area ratio of the Si-O-Si stretching mode was 52.9%, which increased to 60.1, 57.1, and 56.0% following etching under CF_4, $CF_4 + O_2$, and $CF_4 + Ar$, respectively. Likewise, for the films at 60 W, the peak area ratio of the Si-O-Si stretching mode was 55.9%, which increased to 69.5, 63.8, and 66.4% following etching under CF_4, $CF_4 + O_2$, and $CF_4 + Ar$, respectively. The fraction of the Si-O-Si stretching mode increased by the most after etching in CF_4 for both 20 and 60 W. The Si-$(CH_3)_x$ stretching mode had the second largest peak area ratio both before and after etching. For the films at 20 W, the peak area ratio of the Si-$(CH_3)_x$ stretching mode was 40.3%, which decreased to 27.8, 30.4, and 31.4% following etching under CF_4, $CF_4 + O_2$, and $CF_4 + Ar$, respectively. For the films at 60 W, the peak area ratio of the Si-$(CH_3)_x$ stretching mode was 36.9%, which decreased to 21.3, 23.9, and 22.2% following etching under CF_4, $CF_4 + O_2$, and $CF_4 + Ar$, respectively. The films for both 20 and 60 W showed the largest decrease in the fraction of the Si-$(CH_3)_x$ stretching mode after etching in CF_4. The Si-CH_3 bending and CH_x stretching modes had their peak area ratios below 10% after etching for both 20 and 60 W. The peak area ratio for both modes slightly increased following the etching process. As the plasma power increased from 20 to 60 W, overall peak area ratios of the Si-O-Si

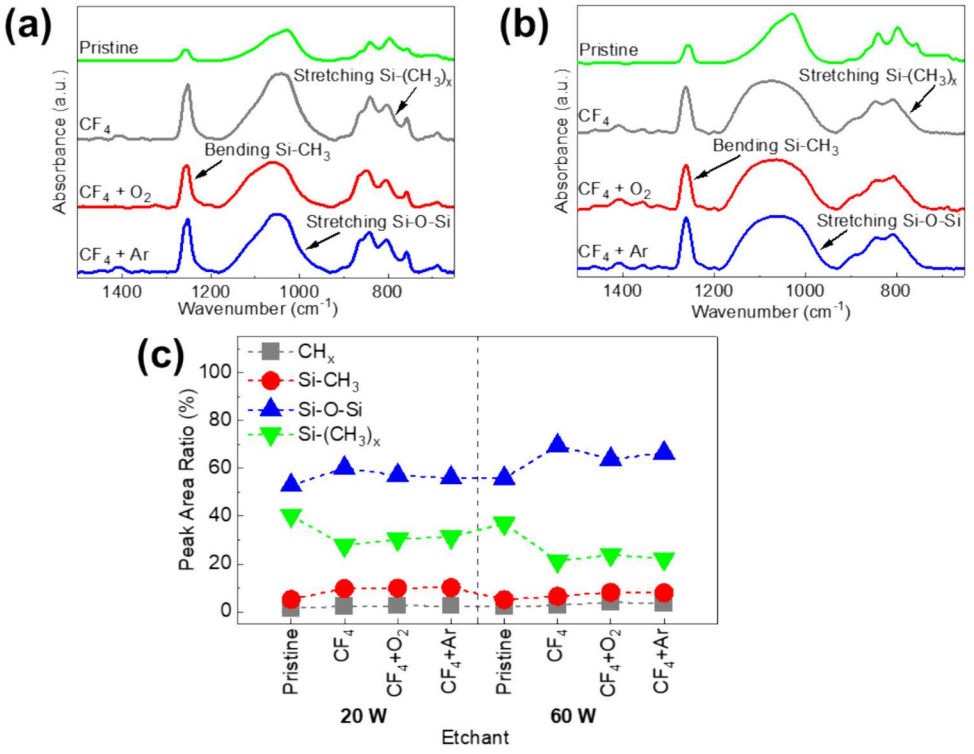

Fig. 4. FTIR spectra of pristine and etched flexible SiCOH thin films at deposition plasma powers of (a) 20 W and (b) 60 W and (c) calculated peak area ratios of four prominent absorption bands. Etching gases were selected among CF_4, $CF_4 + O_2$, and $CF_4 + Ar$.

stretching mode increased while those of the Si-$(CH_3)_x$ stretching mode decreased after etching process. The reduction in the Si-$(CH_3)_x$ stretching mode indicated a removal of the methyl groups by reactive radicals during etching process. More reduction in methyl groups was observed for 60 W, expecting more hydrophilic SiCOH films and thus increased *k*-values.

A series of FTIR spectra stacks which isolate the region of the Si-O-Si stretching, Si-CH_3 bending, Si-$(CH_3)_x$ stretching, and CH_x stretching absorption bands for pristine and etched flexible SiCOH thin films can be seen in the **Supplementary Information (Fig. S2)**. All four peaks changed their shape intensity after etching process. For the Si-O-Si stretching peaks after etching, the peak intensity increased for 20 W while the peak became broader without an increase in the peak intensity. The peak center shifted to higher wavenumbers for both 20 and 60 W. The shape and broadness of the Si-O-Si peak could affect the fraction of constituent peaks of cage, network, and suboxide structures. The peak intensity of the Si-CH_3 bending peak considerably increased after etching. For the Si-$(CH_3)_x$ and CH_x stretching peaks, overall peak intensities increased and the peak shape was changed after etching, possibly causing a change in the peak area ratios of constituent peaks.

Fig. 5(a)-(d) shows the deconvolution of the Si-O-Si stretching, Si-CH_3 bending, Si-$(CH_3)_x$ stretching, and CH_x stretching modes of the flexible SiCOH films after etching under CF_4 plasma as a representative, respectively. The deconvolution of each mode was useful to analyze the change in the chemical structures after etching. The graphs on the top and the bottom for each figure were taken from the films deposited at 20 and 60 W, respectively. The peaks after etching under $CF_4 + O_2$ and $CF_4 + Ar$ were also deconvoluted in the same manner. The Si-O-Si stretching mode was deconvoluted into three peaks of cage, network, and suboxide structures, assigning to their respective wavenumbers of 1135, 1063,

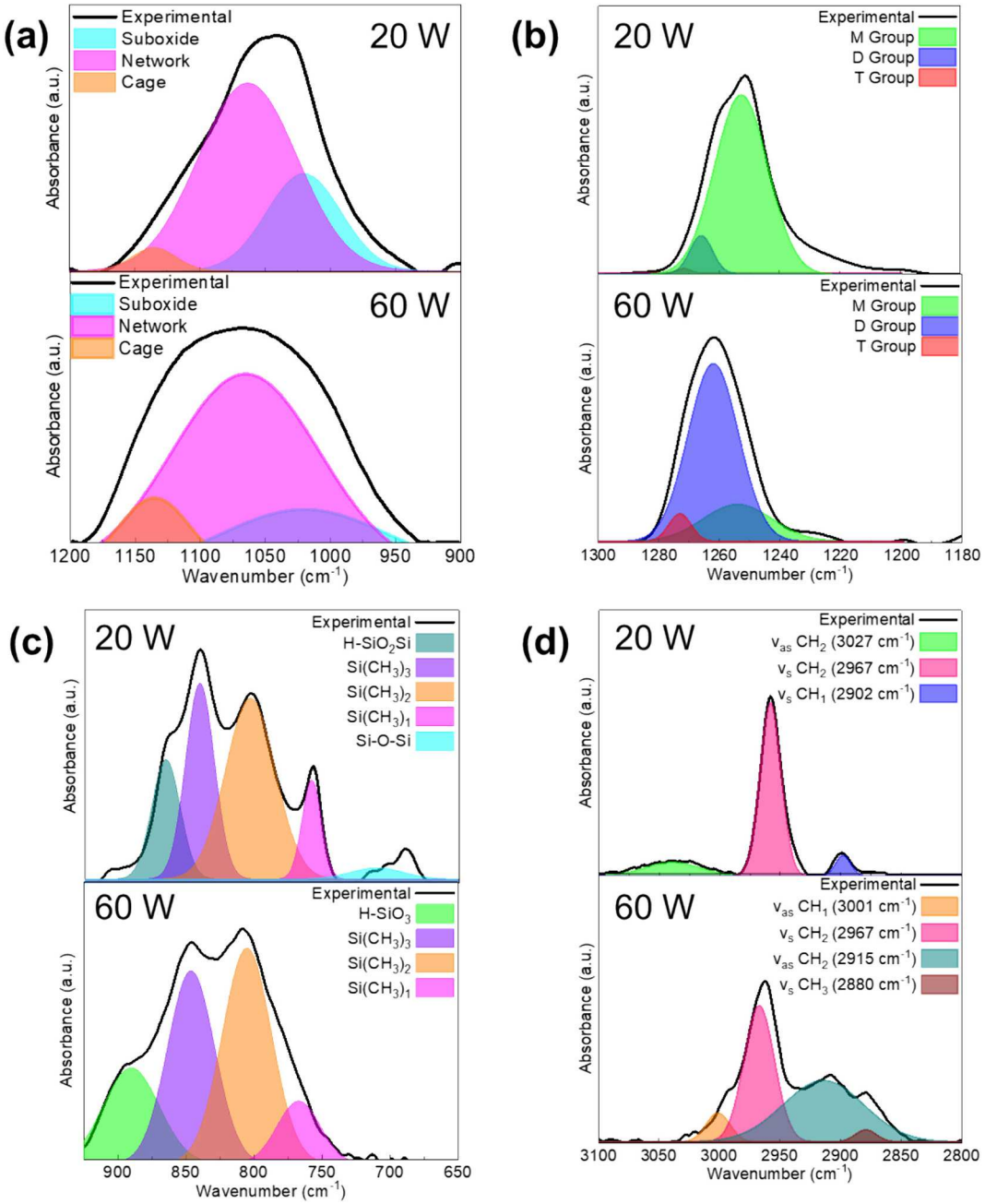

Fig. 5. Deconvolution of FTIR spectra of (a) Si-O-Si stretching, (b) Si-CH_3 bending, (c) Si-$(CH_3)_x$ stretching, and (d) CH_x stretching absorption bands for etched flexible SiCOH thin films using CF_4. Deposition plasma powers were 20 and 60 W.

1023 cm^{-1} [36]. The cage, network, and suboxide peaks approximately corresponded to Si-O-Si bonding angles of 150°, 140°, and <140°, respectively [36]. The dominant structure was the network structure, followed by the suboxide and cage structures for both plasma powers. The Si-CH_3 bending mode was deconvoluted into three peaks of M-, D-, and T-groups assigned to their respective wavenumbers of 1254, 1262, and 1273 cm^{-1} [36,60]. The M-, D-, and T-groups corresponded to O-Si-$(CH_3)_3$, O_2-Si-$(CH_3)_2$, and O_3-Si-CH_3 bond configurations, respectively [34]. They were named based on the bonding state determined by the silicon atom incorporated with the oxygen atoms and the methyl functional groups [61]. The M-group consists of one oxygen atom and three methyl groups connected to a single silicon atom. The D-group is involved with two oxygen atoms and two methyl groups connected to one silicon atom. The T-group consists of three oxygen atoms and one methyl group connected to one silicon atom. The M-group was dominant for the film at 20 W, followed by the D- and T-groups. The D-group was dominant for the film at 60 W, followed by the M- and T-groups. The Si-$(CH_3)_x$ stretching mode was deconvoluted into six peaks: H-SiO_3, H-SiO_2-Si, Si-$(CH_3)_3$, Si-$(CH_3)_2$, Si-$(CH_3)_1$, and Si-O-Si, located at wavenumbers of 890, 865, 840, 803, 758, and 710 cm^{-1}, respectively [27]. The Si-$(CH_3)_2$ peak was most prominent for the films deposited at both plasma powers. The H-SiO_2-Si and Si-O-Si peaks were present only in the film at 20 W. Conversely, the H-SiO_3 peak was present only in the film at 60 W. The Si-$(CH_3)_3$ and Si-$(CH_3)_1$ peaks showed reduced peak intensity and increased broadness as the plasma power increased from 20 to 60 W. The deconvoluted peaks of the CH_x stretching mode varied depending on the deposition plasma power and etching conditions. It was known that the CH_x stretching mode consists of several symmetric (ν_s) and asymmetric (ν_{as}) CH_x stretching modes: ν_{as} CH_2, ν_{as} CH_1, ν_s CH_2, ν_{as} CH_2, ν_{as} CH_2, ν_s CH_1, ν_s CH_3, and ν_s CH_2 modes at their corresponding wavenumbers of 3027, 3001, 2967, 2933, 2915, 2902, 2880, and 2857 cm^{-1} [62,63]. The SiCOH film at 20 W etched in CF_4 showed ν_{as} CH_2, ν_s CH_2, and ν_s CH_1 modes at wavenumbers of 3027, 2967, and 2902 cm^{-1}, respectively. In comparison, The SiCOH film at 60 W etched in CF_4 showed ν_{as} CH_1, ν_s CH_2, ν_{as} CH_2, and ν_s CH_3 modes at wavenumbers of 3001, 2967, 2915, and 2880 cm^{-1}, respectively. A large fraction of the deconvoluted peak was ν_s CH_2 and ν_{as} CH_2 for 20 and 60 W, respectively. The constituent peaks of four prominent peaks after each deconvolution were varied depending etching conditions and are explained with peak area ratios as shown in Fig. 6 and in the **Supplementary Information (Fig. S3)**.

Fig. 6(a) and (b) shows the peak area ratios of the deconvoluted absorption peaks of the Si-O-Si stretching mode for the pristine and etched flexible SiCOH films deposited at 20 and 60 W, respectively. For the films at 20 W, the pristine film had a similar fraction for the suboxide and network structures at 48.4 and 47.6%, respectively, with a small fraction of the cage structure below 4.0%. The cage structure did not change its fraction after etching. Etching under CF_4 plasma caused the fraction of the suboxide structure to decrease from 48.4 to 27.0%, while the fraction of the network structure increased from 47.6 to 69.1%. The addition of Ar or O_2 to the plasma caused the fraction of the suboxide structure to decrease substantially to 13.0 and 2.7%, respectively. Conversely, the addition of Ar or O_2 caused the fraction of the network structure to increase to 85.7 and 92.2%, respectively. For the films at 60 W, the pristine film had a dominant suboxide structure followed by network and cage structures. The fraction of the cage structure decreased after etching. The suboxide structure was dominant for the pristine film with a fraction of 52.9%, but the etched films displayed significantly decreased fractions, down to 23.1, 7.2, and 5.5% under CF_4, CF_4 + O_2, and CF_4 + Ar, respectively. The network structure had a

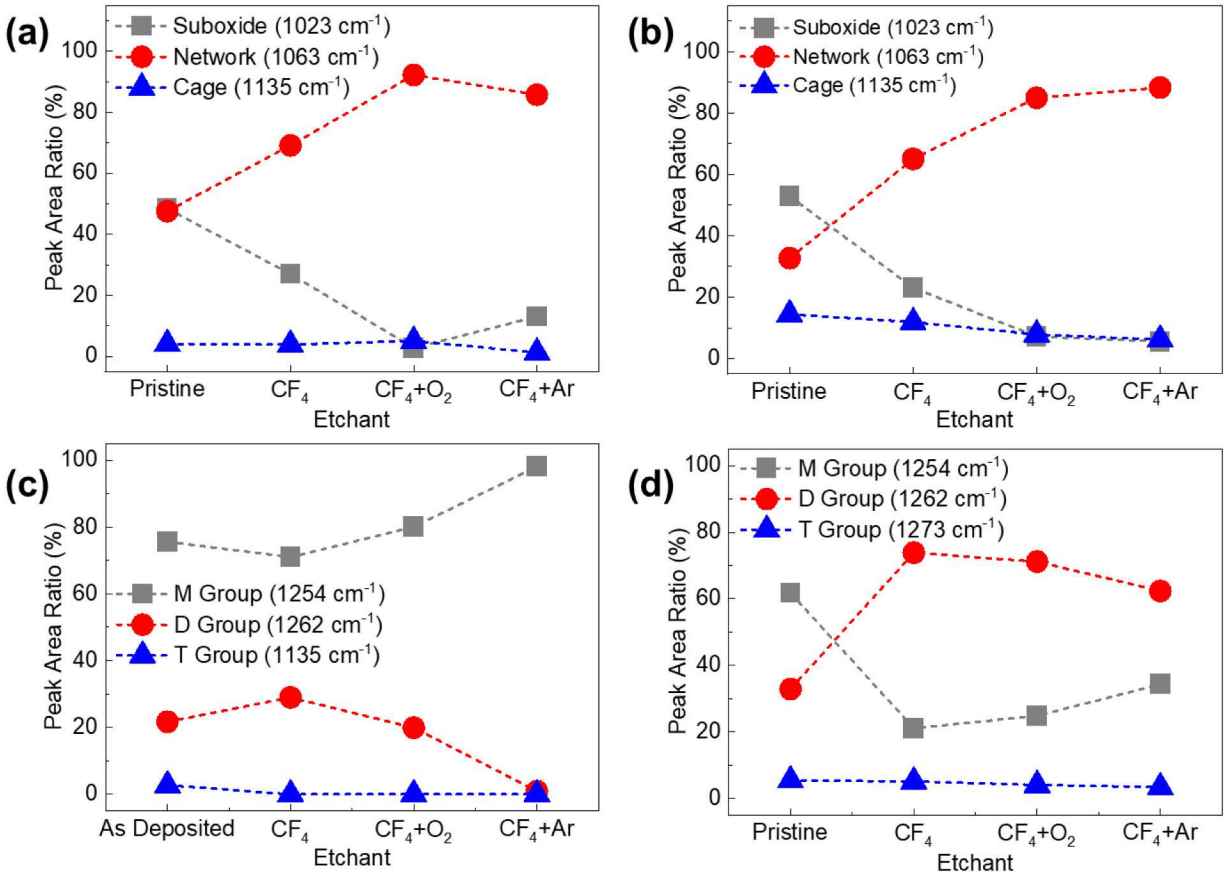

Fig. 6. Peak area ratios for deconvoluted absorption bands of Si-O-Si for etched flexible SiCOH thin films for the deposition plasma powers of (a) 20 and (b) 60 W and Si-CH_3 for etched flexible SiCOH thin films deposited at (c) 20 and (d) 60 W. Etching gases were selected among CF_4, CF_4 + O_2, and CF_4 + Ar.

fraction of 32.7% for the pristine film, which increased significantly to 65.0, 85.0, and 88.3% under etching in CF_4, $CF_4 + O_2$, and $CF_4 + Ar$, respectively. The network structure of the films was most dominant after etching under $CF_4 + Ar$. Overall, the portion of the network structure increased and the portion of the suboxide decreased after etching for both 20 and 60 W. Fig. 6(c) and (d) shows the peak area ratios of the deconvoluted absorption peaks of the Si-CH_3 bending mode for the pristine and etched flexible SiCOH films deposited at 20 and 60 W, respectively. For the pristine film at 20 W, the M-group was dominant at 75.6%, followed by the D- and T-groups at 21.7 and 2.7%, respectively. The peak area ratio of the M-group increased to 75.6, 80.1, and 98.1% after etching under CF_4, $CF_4 + O_2$, and $CF_4 + Ar$, respectively. Conversely, the peak area ratio of the D-group decreased to 29.0, 19.9, and 1.9% after etching under CF_4, $CF_4 + O_2$, and $CF_4 + Ar$, respectively. The M-group was still dominant following etching. Interestingly, the T-group disappeared after etching. For the pristine film at 60 W, the M-group was dominant at 61.7%, followed by the D- and T-groups at 32.9 and 5.4%, respectively. The peak area ratio of the M-group decreased substantially to 21.1, 24.8, and 34.3% after etching under CF_4, $CF_4 + O_2$, and $CF_4 + Ar$, respectively. Conversely, the peak area ratio of the D-group increased substantially to 73.8, 71.1, and 62.3 after etching under CF_4, $CF_4 + O_2$, and $CF_4 + Ar$, respectively. The peak area ratio of the T-group was not changed much after the etching process. For both pristine films at 20 and 60 W, the M-group was dominant. After etching process, the M-group was still dominant for the film at 20 W, but the M-group became recessive, and the D-group was prominent for the film at 60 W. The increased peak area ratio of the D-group after etching of the films at 60 W indicated that methyl groups were removed by the etching process. This corresponded with increased refractive index values observed for the films at 60 W after etching, as the removal of methyl groups allowed for more cross-linking within the films. Additionally, the significant reduction of contact angle observed for the films at 60 W after etching was associated with the reduction in methyl groups observed from the increased prominence of the D-group [59].

The peak area ratios of the deconvoluted absorption peaks of the Si-$(CH_3)_x$ and CH_x stretching modes for the pristine and etched flexible SiCOH films can be seen in the **Supplementary Information (Fig. S3)**.

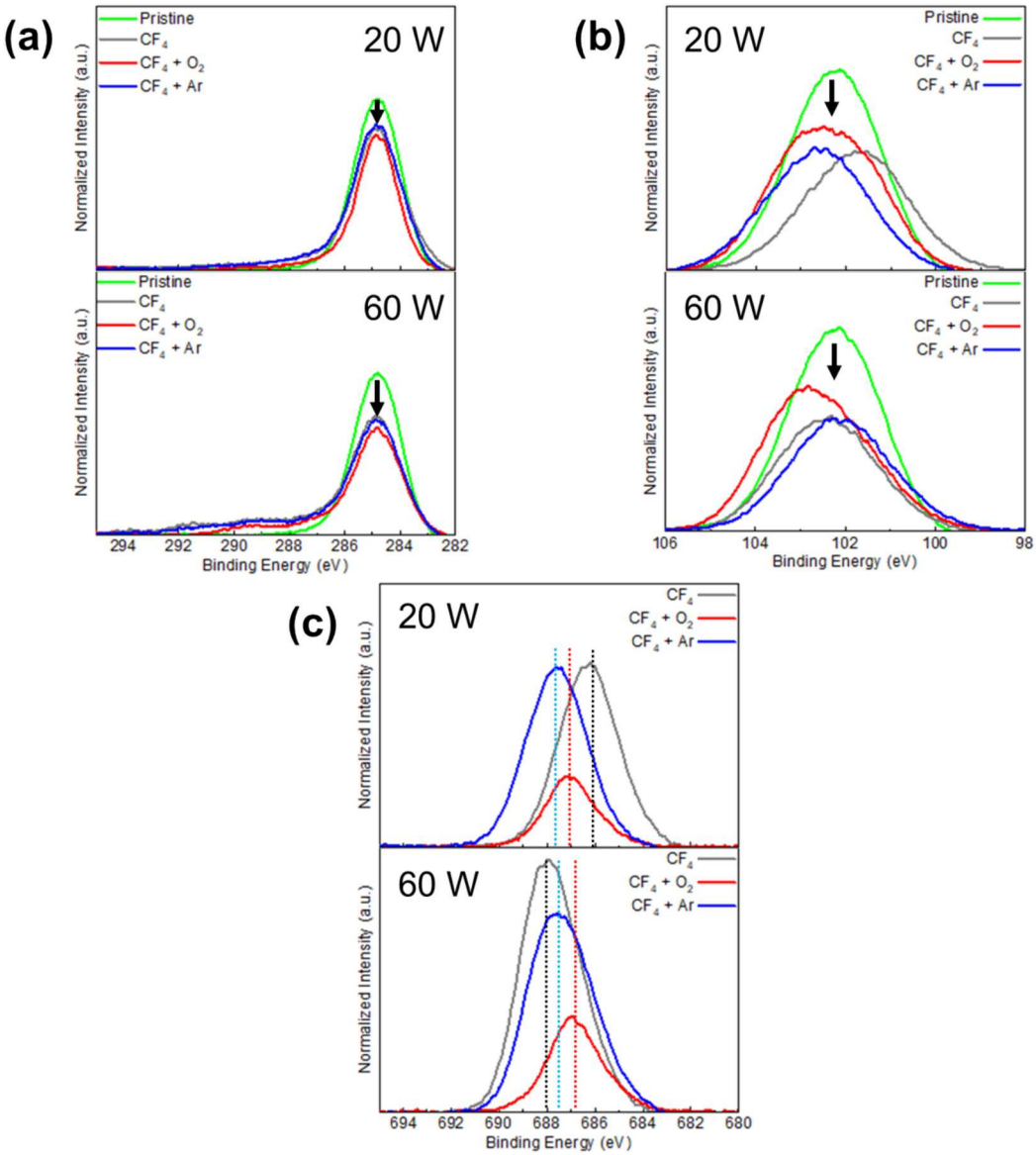

Fig. 7. XPS spectra stack of (a) C1s, (b) Si2p, and (c) F1s peaks of pristine and etched SiCOH thin films using various etch gases for the deposition plasma powers of 20 and 60 W.

3.4. XPS analysis

The chemical bond structure and elemental composition of the flexible SiCOH thin films before and after etching were determined using an XPS analysis. From the XPS survey scans, four prominent peaks were identified as F1s (~688 eV), O1s (~533 eV), C1s (284.8 eV), and Si2p (~150 eV) [40,46]. A peak identified as Si2s (~250 eV) was also found with a low intensity. The O KLL (~980 eV) and F KLL (~830 eV) peaks were attributed to Auger electron emission related to oxygen and fluorine, respectively [64]. The F1s peak became present in the SiCOH thin films following etching, resulting from the interaction between the CF_4 etching gas and the film.

Fig. 7(a)-(c) presents the XPS spectra stack of C1s, Si2p, and F1s peaks of pristine and etched SiCOH thin films using various etch gases, respectively. The graphs on the top and the bottom for each figure were taken from the films deposited at 20 and 60 W, respectively. The peak intensity of both C1s and Si2p peaks was depressed after etching for both 20 and 60 W. The peak intensity of F1s peak was much greater for the film etched under CF_4 and CF_4 + Ar etching gases than for the film etched under $CF_4 + O_2$. It is probable that the film was more interactive with oxygen radicals than fluorine radicals, resulting in suppressed F1s peak. While the peak center of the C1s peak stayed almost constant, the Si2p peak shifted its peak center to a lower binding energy within a range of 0.203–0.953 eV except for etching in CF_4 for 20 W. The largest shift of 0.953 eV was observed for etching in $CF_4 + O_2$ at 60 W. The peak center of the F1s peak was different depending on etching conditions. The peak centers of the F1s for etching in CF_4 were 686.2 and 687.9 eV for 20 and 60 W, respectively. When Ar or O_2 was added to CF_4, the peak center shifted to a higher binding energy for 20 W and to a lower binding energy for 60 W. For example, the peak shifted to a higher binding energy with 1.4 eV for the film at 20 W after etching in $CF_4 + Ar$ and to a lower binding energy with 1.0 eV for the film at 60 W after etching in $CF_4 + O_2$. It is possible that the shift of the F1s peak was due to formation of fluorine compounds due to the interaction between etching gas and the film surface.

Fig. 8(a) and (b) shows the atomic concentrations of the flexible SiCOH films before and after etching for the films deposited at 20 and 60 W, respectively. The atomic concentration of the films was calculated using the peak area ratio of the four prominent peaks of Si2p, C1s, O1s, and F1s found in the XPS high-resolution scans. To investigate the difference in elemental composition between the surface layer and the bulk material, additional high-resolution scans of four peaks were performed after 2 min of Ar ion sputtering. After etching process, fluorine concentration was observed and more fluorine was found for 60 W. The elemental composition of the pristine SiCOH film at 20 W was 43.4% carbon, 37.4% silicon, and 19.2% oxygen. While the carbon content of the films etched under CF_4 and CF_4 + Ar remained almost the same, the carbon concentration of the film etched under $CF_4 + O_2$ decreased to 29.3%. The concentration of silicon decreased to 24.6, 30.6, and 24.8% for the films etched under CF_4, $CF_4 + O_2$, and CF_4 + Ar, respectively. The oxygen concentration of the film etched under $CF_4 + O_2$ significantly increased to 35.6%, but remained almost consistent between the pristine film and the films etched under CF_4 and CF_4 + Ar. The fluorine concentrations of 14.2 and 14.1% were found in the films following etching under CF_4 and CF_4 + Ar, respectively. Interestingly, a smaller fluorine concentration of 4.5% was observed after etching under $CF_4 + O_2$. It is likely that oxygen radicals are more reactive with the film compared to fluorine radicals. Following the 2 min of Ar ion sputtering process, the atomic concentrations of the etched films were comparable to those of the pristine film at 20 W although the etched film in $CF_4 + O_2$ showed some deviation from the pristine concentrations. A small concentration of fluorine (~1%) was still detected within the etched films following the Ar sputtering. The elemental composition of the pristine SiCOH film at 60 W was 41.0% carbon, 39.0% silicon, and 20.0% oxygen. Slightly lower carbon concentration was obtained, compared to the film at 20 W. The carbon concentration of the film etched under $CF_4 + O_2$ decreased to 28.1%, but remained consistent between the pristine film and the films etched under CF_4 and CF_4 + Ar. The concentration of silicon decreased to 21.3, 28.3, and 22.2% for the films etched under CF_4, $CF_4 + O_2$, and CF_4 + Ar, respectively. The oxygen concentration significantly increased to 37.6% for the film etched under $CF_4 + O_2$ but slightly increased within ~2% for the films etched under CF_4 and CF_4 + Ar. Fluorine concentrations of 18.2 and 17.1% were found for the films etched under CF_4 and CF_4 + Ar, respectively, while a smaller concentration of fluorine of 6.0% was found for the film etched under $CF_4 + O_2$. Similar to the films at 20 W, the atomic concentrations of the pristine and etched films at 60 W were comparable following the 2 min of Ar ion sputtering. A small concentration of fluorine (~1%) was detected within the etched films following the Ar sputtering.

It was known that damage of the SiCOH film is the result of a competition between the etch rate and the diffusion rate of active species such as O and F. The diffusion of the etching species to the film should stop at some point. The sputtered depth through the 2 min of Ar ion sputtering was speculated around 10–30 nm. From the elemental analysis after the sputtering, all elemental compositions of C, Si, and O were almost recovered to those of the pristine film. Thus,

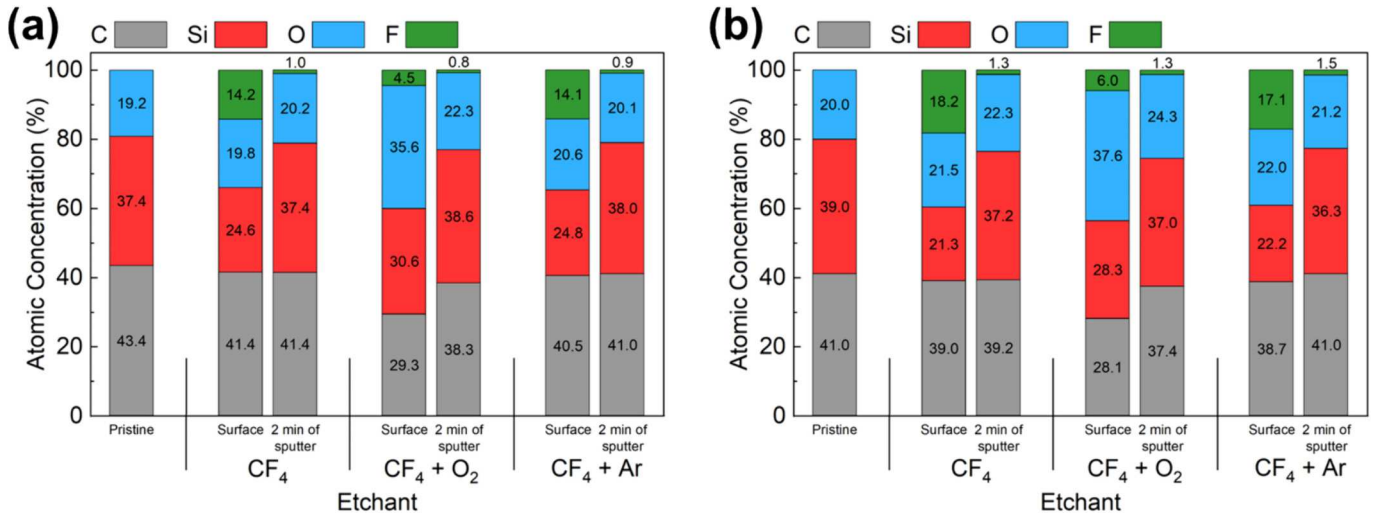

Fig. 8. Atomic concentrations of pristine and etched flexible SiCOH thin films using various etching gases for deposition plasma powers of (a) 20 and (b) 60 W. Atomic concentrations of etched films were measured additionally after 2 min of Ar ion sputtering.

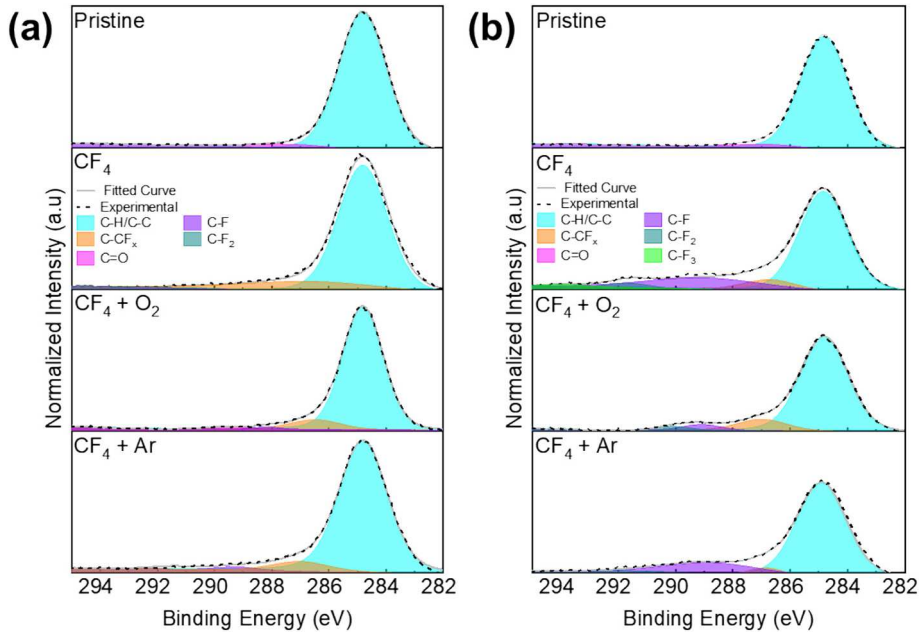

Fig. 9. Deconvolution of the C1s peaks for pristine and etched flexible SiCOH thin films using various etching gases for deposition plasma powers of (a) 20 and (b) 60 W.

physicochemical modification or damage may appear at the top surface of the film, over the depth of around 10–30 nm.

Fig. 9(a) and (b) presents the deconvolution of the C1s peaks for the flexible SiCOH films deposited at 20 and 60 W, respectively, before and after etching. The C1s peak was deconvoluted into six peaks of C-H/C-C, C-CF_x, C═O, C—F, C—F_2, and C—F_3, located at approximate binding energies of 284.8, 286.4, 287.6, 289.2, 291.4, and 293.8 eV, respectively [41,45,46,65]. Their peak area ratios were also calculated. For the pristine film at 20 W, the C-H/C-C peak was dominant with the peak area ratio of 93.4%, followed by the C═O peak with 6.6%. The etched films showed the incorporation of fluorine atoms into the film structure, indicating the formation of a fluorocarbon layer during the etching process. This resulted in appearance of fluorocarbon peaks such as C-CF_x, C—F, and C—F_2 peaks except C—F_3 peak. The dominant C-H/C-C peak showed the reduction in the peak area ratios of 79.7, 88.4, and 87.6% after etching in CF_4, $CF_4 + O_2$, and $CF_4 + Ar$, respectively. The peak area ratios of the C-CF_x peak were 19.6, 8.9, and 8.1% for etching in CF_4, $CF_4 + O_2$, and $CF_4 + Ar$, respectively. The rest of fluorocarbon peaks had their peak area ratios below 2.3%. The C═O peak was observed with <1.1% for all etching conditions. For the pristine film at 60 W, the C-H/C-C peak was dominant with the peak area ratio of 93.5%, followed by the C═O peak with 6.5%. Compared to the film at 20 W, the dominant C-H/C-C peak showed the further reduction in the peak area ratios of 69.0, 82.6, and 74.4% after etching in CF_4, $CF_4 + O_2$, and $CF_4 + Ar$, respectively. All fluorocarbon peaks were detected for etching in CF_4 and three of them except C—F_3 were for etching in $CF_4 + O_2$ and $CF_4 + Ar$. The peaks with the largest area ratio among the fluorocarbon peaks were C—F for CF_4 and $CF_4 + Ar$ with their respective ratios of 19.1 and 18.4% and C-CF_x for $CF_4 + O_2$ with 10.7%. The C═O peak was not observed for all etching conditions.

The deconvolution of the Si2p peak for the flexible SiCOH films before and after etching can be seen in the **Supplementary Information (Fig. S4)**. The Si2p peak was deconvoluted into three peaks of M-, D-, and T-groups assigned to their binding energies of 101.9, 102.9, and 103.7 ± 0.1 eV, respectively [30]. The M-, D-, and T-groups were attributed to O-Si-C_3, O_2-Si-C_2, and O_3-Si-C bonding configurations, respectively. Their peak area ratios were also calculated. The constituent bonding configuration of the Si2p peak was considerably affected by both the film composition and the etching gas mixture.

As stated previously, an F1s peak was observed in the XPS spectra of the SiCOH thin films following etching due to interactions between the CF_4 etching gas and the film. The deconvolution of the F1s peaks for etched flexible SiCOH thin films using various etching gases can be seen in the **Supplementary Information (Fig. S5)**. The F1s peak was deconvoluted into three peaks of C—F, C—F_2, and C—F_3 with their respective binding energies of 686.3–686.9, 687.3–689.1, and 690.7–691.1 eV. The deconvolution of the F1s peak was compared to that of the C1s peak to support the validity of its results. In the deconvolution of the C1s peak, C-CF_x, C—F, and C—F_2 were found with a main portion of C-H/C-C for both 20 and 60 W and only C—F_3 was found in etching in CF_4 for 60 W. This aligned with the results of the peak deconvolution of the F1s peak and demonstrated that the results from the C1s and F1s peak analysis were well matched.

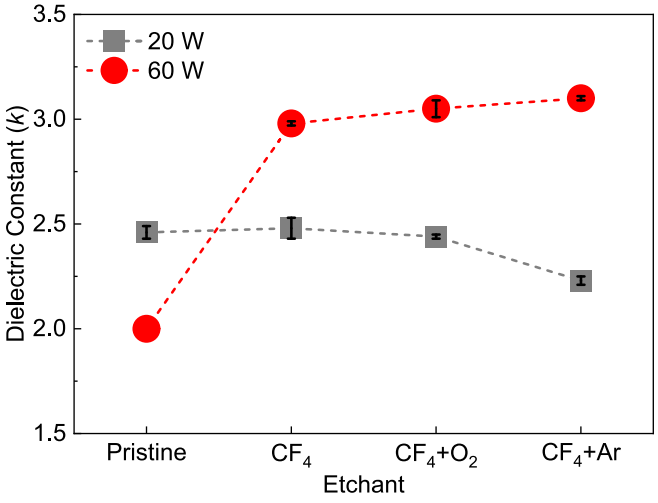

Fig. 10. Dielectric constant of pristine and etched flexible SiCOH thin films using various etching gases for deposition plasma powers of 20 and 60 W.

3.5. Dielectric constant

Fig. 10 shows the dielectric constant (k) for the pristine and etched flexible SiCOH thin films. The pristine film at 20 W had a k-value of 2.46, while the films etched under CF_4, $CF_4 + O_2$, and $CF_4 + Ar$ had values of 2.48, 2.44, and 2.23, respectively. The k-values of the SiCOH films at 20 W were not much affected by etching process. The pristine film at 60 W had the k-value of 2.00. The k-values of the films at 60 W increased substantially following the etching process and were 2.98, 3.05, and 3.10 for CF_4, $CF_4 + O_2$, and $CF_4 + Ar$, respectively. The increase in the k-values of the etched 60 W films could be caused by possible plasma damage to the film during the reaction between the etching species and the film [44,66]. Evidence of plasma damage in the films at 60 W after etching was expressed in the contact angle, refractive index, and FTIR results. Plasma damage resulted in the removal of methyl groups from the etched films, as observed by the increased dominance of the D-group from the deconvolution of the Si-CH_3 peak of FTIR. The reduction of methyl groups corresponded increased surface hydrophilicity [59]. Additionally, the reduction of methyl groups allowed for increased cross-linking within the film, increasing its density and thus its refractive index. It was known that the increase in the refractive index induces the increased k-values [54,55]. The SiCOH films at 20 W had little change in the refractive index whereas the films at 60 W showed the increased refractive index after the etching process. The increased refractive index after etching resulted in higher k-values. Lastly, the change in the peak area ratios from the FTIR spectra were different for the films at 20 and 60 W. After the etching process, the peak area ratios of two major peaks of Si-O-Si and Si-$(CH_3)_x$ for the film at 20 W increased by 3.1–7.2% and decreased by 8.9–12.5%, respectively. In comparison, the peak area ratios of Si-O-Si and Si-$(CH_3)_x$ for the films at 60 W increased by 7.9–13.6% and decreased by 13.0–15.6%, respectively, after etching. It is possible that the increased fraction of dominant chemical configurations resulted from the etching process led to higher k-values.

4. Conclusions

The flexible SiCOH thin films onto ITO/PEN substrates were prepared by PECVD of the TTMSS precursor at deposition plasma powers of 20 and 60 W, and the chemical structures of the films were investigated after ICP-RIE process under CF_4, $CF_4 + O_2$, and $CF_4 + Ar$. After the etching process, the refractive index of the films at 20 W remained unchanged while the films at 60 W showed the increased refractive index. The contact angles decreased considerably decreased following the etching process, many of the etched films being hydrophilic. The FTIR spectra identified prominent absorption bands as Si-O-Si stretching, Si-$(CH_3)_x$ stretching, Si-CH_3 bending, and CH_x stretching vibration modes. The etching process induced the increase in the fraction of Si-O-Si stretching mode and the decrease in the fraction of Si-$(CH_3)_x$ stretching mode, indicating the removal of methyl groups from the film. It is notable that the SiCOH films at 60 W after etching showed evidence of increased methyl group removal, both from a decrease in the amount of Si-$(CH_3)_x$ and from an analysis of the Si-CH_3 deconvolution. The peak area ratio analysis from the XPS C1s, Si2p, and F1s spectra demonstrated that the bonding configuration was substantially affected by the etching process. All etched films showed a significant concentration of fluorine, indicating the formation of a fluorocarbon layer. The k-values of the films at 20 W were insensitive to etching conditions while those of the films at 60 W increased substantially following etching. The increase in the k-values after the etching process was directly associated with the change in chemical configuration, surface wettability, and refractive index. The insensitivity of the flexible SiCOH films deposited at 20 W to various etching conditions is advantageous for their use as inter-metal dielectrics and demonstrates that the traditional dry etching procedures remain applicable for flexible electronic device fabrication.

Ethical statement

Research results are not misrepresented. The results are presented clearly, honestly and without fabrication, falsification or inappropriate data manipulation. The results are appropriately placed in the context of prior and existing research. No data, text, or theories by others are presented as if they were the author's own.

This is the authors' own original work, which has not been previously published elsewhere. The manuscript is not currently being considered for publication elsewhere. The manuscript reflects the authors' own research and analysis in a truthful and complete manner.

The manuscript properly credits the meaningful contributions of co-authors. All authors have been personally and actively involved in substantial work leading to the manuscript and will take public responsibility for its content.

Declaration of competing interest

The authors declare that they have no known competing financial interests or personal relationships that could have appeared to influence the work reported in this paper.

Seonhee Jang reports financial support was provided by National Science Foundation. If there are other authors, they declare that they have no known competing financial interests or personal relationships that could have appeared to influence the work reported in this paper.

Data availability

The data that support the findings of this study are available from the corresponding author upon reasonable request.

Acknowledgements

This work was supported by the National Science Foundation under Grant No. CMMI 2026801. The authors would like to thank the Nanofabrication Facility at Louisiana State University for use of nanofabrication equipment.

Appendix A. Supplementary data

Supplementary data to this article can be found online at https://doi.org/10.1016/j.mee.2024.112221.

References

[1] B.D. Gates, Flexible electronics, Science 323 (2009) 1566–1567, https://doi.org/10.1126/science.1171230.
[2] A. Nathan, A. Ahnood, M.T. Cole, Sungsik Lee, Y. Suzuki, P. Hiralal, F. Bonaccorso, T. Hasan, L. Garcia-Gancedo, A. Dyadyusha, S. Haque, P. Andrew, S. Hofmann, J. Moultrie, Daping Chu, A.J. Flewitt, A.C. Ferrari, M.J. Kelly, J. Robertson, G.A. J. Amaratunga, W.I. Milne, Flexible electronics: The next ubiquitous platform, Proc. IEEE 100 (2012) 1486–1517, https://doi.org/10.1109/JPROC.2012.2190168.
[3] D. Corzo, G. Tostado-Blázquez, D. Baran, Flexible electronics: status, challenges and opportunities, Front. Electron. 1 (2020) 594003, https://doi.org/10.3389/felec.2020.594003.
[4] M.-C. Choi, Y. Kim, C.-S. Ha, Polymers for flexible displays: from material selection to device applications, Prog. Polym. Sci. 33 (2008) 581–630, https://doi.org/10.1016/j.progpolymsci.2007.11.004.
[5] R. Manda, S. Pagidi, Y.J. Lim, R. He, S.M. Song, J.H. Lee, G.-D. Lee, S.H. Lee, Self-supported liquid crystal film for flexible display and photonic applications, J. Mol. Liq. 291 (2019) 111314, https://doi.org/10.1016/j.molliq.2019.111314.
[6] Y. Wu, Y. Ma, H. Zheng, S. Ramakrishna, Piezoelectric materials for flexible and wearable electronics: a review, Mater. & Des. 211 (2021) 110164, https://doi.org/10.1016/j.matdes.2021.110164.
[7] C. Zhu, J. Wu, J. Yan, X. Liu, Advanced fiber materials for wearable electronics, Adv. Fiber Mater. 5 (2023) 12–35, https://doi.org/10.1007/s42765-022-00212-0.
[8] X. Li, P. Li, Z. Wu, D. Luo, H.-Y. Yu, Z.-H. Lu, Review and perspective of materials for flexible solar cells, Mater. Reports: Energy 1 (2021) 100001, https://doi.org/10.1016/j.matre.2020.09.001.
[9] H.S. Jung, G.S. Han, N.-G. Park, M.J. Ko, Flexible perovskite solar cells, Joule 3 (2019) 1850–1880, https://doi.org/10.1016/j.joule.2019.07.023.

[10] Y. Luo, M.R. Abidian, J.-H. Ahn, D. Akinwande, A.M. Andrews, M. Antonietti, Z. Bao, M. Berggren, C.A. Berkey, C.J. Bettinger, J. Chen, P. Chen, W. Cheng, X. Cheng, S.-J. Choi, A. Chortos, C. Dagdeviren, R.H. Dauskardt, C. Di, M. D. Dickey, X. Duan, A. Facchetti, Z. Fan, Y. Fang, J. Feng, X. Feng, H. Gao, W. Gao, X. Gong, C.F. Guo, X. Guo, M.C. Hartel, Z. He, J.S. Ho, Y. Hu, Q. Huang, Y. Huang, F. Huo, M.M. Hussain, A. Javey, U. Jeong, C. Jiang, X. Jiang, J. Kang, D. Karnaushenko, A. Khademhosseini, D.-H. Kim, I.-D. Kim, D. Kireev, L. Kong, C. Lee, N.-E. Lee, P.S. Lee, T.-W. Lee, F. Li, J. Li, C. Liang, C.T. Lim, Y. Lin, D. J. Lipomi, J. Liu, K. Liu, N. Liu, R. Liu, Y. Liu, Y. Liu, Z. Liu, Z. Liu, X.J. Loh, N. Lu, Z. Lv, S. Magdassi, G.G. Malliaras, N. Matsuhisa, A. Nathan, S. Niu, J. Pan, C. Pang, Q. Pei, H. Peng, D. Qi, H. Ren, J.A. Rogers, A. Rowe, O.G. Schmidt, T. Sekitani, D.-G. Seo, G. Shen, X. Sheng, Q. Shi, T. Someya, Y. Song, E. Stavrinidou, M. Su, X. Sun, K. Takei, X.-M. Tao, B.C.K. Tee, A.V.-Y. Thean, T.Q. Trung, C. Wan, H. Wang, J. Wang, M. Wang, S. Wang, T. Wang, Z.L. Wang, P.S. Weiss, H. Wen, S. Xu, T. Xu, H. Yan, X. Yan, H. Yang, L. Yang, S. Yang, L. Yin, C. Yu, G. Yu, J. Yu, S.-H. Yu, X. Yu, E. Zamburg, H. Zhang, X. Zhang, X. Zhang, X. Zhang, Y. Zhang, Y. Zhang, S. Zhao, X. Zhao, Y. Zheng, Y.-Q. Zheng, Z. Zheng, T. Zhou, B. Zhu, M. Zhu, R. Zhu, Y. Zhu, Y. Zhu, G. Zou, X. Chen, Technology roadmap for flexible sensors, ACS Nano 17 (2023) 5211–5295, https://doi.org/10.1021/acsnano.2c12606.

[11] Y.-F. Liu, M.-H. An, Y.-G. Bi, D. Yin, J. Feng, H.-B. Sun, Flexible efficient top-emitting organic light-emitting devices on a silk substrate, IEEE Photon. J. 9 (2017) 1–6, https://doi.org/10.1109/jphot.2017.2740618.

[12] S. Park, S.W. Heo, W. Lee, D. Inoue, Z. Jiang, K. Yu, H. Jinno, D. Hashizume, M. Sekino, T. Yokota, K. Fukuda, K. Tajima, T. Someya, Self-powered ultra-flexible electronics via nano-grating-patterned organic photovoltaics, Nature 561 (2018) 516–521, https://doi.org/10.1038/s41586-018-0536-x.

[13] Y.-F. Liu, J. Feng, Y.-G. Bi, D. Yin, H.-B. Sun, Recent developments in flexible organic light-emitting devices, Adv. Mater. Technol. 4 (2019) 1800371, https://doi.org/10.1002/admt.201800371.

[14] P.K. Nair, M.T.S. Nair, Prospects of chemically deposited Cds thin films in solar cell applications, Sol. Cells. 22 (1987) 103–112, https://doi.org/10.1016/0379-6787(87)90050-0.

[15] C.C. Wu, S.D. Theiuss, G. Gu, M.H. Lu, J.C. Sturm, S. Wagner, S.R. Forrest, Integration of organic LEDs and amorphous Si TFTs onto flexible and lightweight metal foil substrates, IEEE Electron Device Lett. 18 (1997) 609–612, https://doi.org/10.1109/55.644086.

[16] P.S. Maydannik, T.O. Kääriäinen, K. Lahtinen, D.C. Cameron, M. Söderlund, P. Soininen, P. Johansson, J. Kuusipalo, L. Moro, X. Zeng, Roll-to-roll atomic layer deposition process for flexible electronics encapsulation applications, J. Vac. Sci. & Technol. A 32 (2014) 051603, https://doi.org/10.1116/1.4893428.

[17] R. He, T.D. Day, J.R. Sparks, N.F. Sullivan, J.V. Badding, High pressure chemical vapor deposition of hydrogenated amorphous silicon films and solar cells, Adv. Mater. 28 (2016) 5939–5942, https://doi.org/10.1002/adma.201600415.

[18] K. Jain, M. Klosner, M. Zemel, S. Raghunandan, Flexible electronics and displays: high-resolution, roll-to-roll, projection lithography and photoablation processing technologies for high-throughput production, Proc. IEEE 93 (2005) 1500–1510, https://doi.org/10.1109/jproc.2005.851505.

[19] K.S. Kim, K.H. Kim, Y.J. Ji, J.W. Park, J.H. Shin, A.R. Ellingboe, G.Y. Yeom, Silicon nitride deposition for flexible organic electronic devices by VHF (162 MHz)-PECVD using a multi-tile push-pull plasma source, Sci. Rep. 19 (2017) 13585, https://doi.org/10.1038/s41598-017-14122-4.

[20] J. Du, B. Tong, S. Yuan, N. Dai, R. Liu, D. Zhang, H.M. Cheng, W. Ren, Advances in flexible optoelectronics based on chemical vapor deposition-grown graphene, Adv. Funct. Mater. 32 (2022) 2203115, https://doi.org/10.1002/adfm.202203115.

[21] G. Hernandez-Sosa, S. Tekoglu, S. Stolz, R. Eckstein, C. Teusch, J. Trapp, U. Lemmer, M. Hamburger, N. Mechau, The compromises of printing organic electronics: a case study of gravure-printed light-emitting electrochemical cells, Adv. Mater. 26 (2014) 3235–3240, https://doi.org/10.1002/adma.201305541.

[22] Y. Khan, A. Thielens, S. Muin, J. Ting, C. Baumbauer, A.C. Arias, A new frontier of printed electronics: flexible hybrid electronics, Adv. Mater. 32 (2020) 1905279, https://doi.org/10.1002/adma.201905279.

[23] W. Volksen, R.D. Miller, G. Dubois, Low dielectric constant materials, Chem. Rev. 110 (2010) 56–110, https://doi.org/10.1021/cr9002819.

[24] K. Maex, M.R. Baklanov, D. Shamiryan, F. Lacopi, S.H. Brongersma, Z. S. Yanovitskaya, Low dielectric constant materials for microelectronics, J. Appl. Phys. 93 (2003) 8793–8841, https://doi.org/10.1063/1.1567460.

[25] S.M. Merchant, S.H. Kang, M. Sanganeria, B. van Schravendijk, T. Mountsier, Copper interconnects for semiconductor devices, JOM 53 (2001) 43–48, https://doi.org/10.1007/s11837-001-0103-y.

[26] H. Kim, M.H. Ha, D. Jung, H. Chae, H. Kim, Effects of He(90%)/H2(10%) plasma treatment on electric properties of low dielectric constant SiCOH films, Mater. Res. Bull. 47 (2012) 3008–3010, https://doi.org/10.1016/j.materresbull.2012.04.097.

[27] Y. Park, H. Lim, S. Kwon, W. Ban, S. Jang, D. Jung, Ultralow dielectric constant SiCOH films by plasma enhanced chemical vapor deposition of decamethylcyclopentasiloxane and tetrakis(trimethylsilyloxy)silane precursors, Thin Solid Films 727 (2021) 138680, https://doi.org/10.1016/j.tsf.2021.138680.

[28] M. Darnon, N. Casiez, T. Chevolleau, G. Dubois, W. Volksen, T.J. Frot, R. Hurand, T.L. David, N. Posseme, N. Rochat, C. Licitra, Impact of low-k structure and porosity on etch processes, J. Vac. Sci. & Technol. B 31 (2013) 011207, https://doi.org/10.1116/1.4770505.

[29] Y. Cho, J. Huang, Z. Zhang, K. Wang, P. Lee, C. Kim, K. Wong, S. Nemani, E. Yieh, A.C. Kummel, Inherent selective pulsed chemical vapor deposition of aluminum oxide in nm scale, Appl. Surf. Sci. 622 (2023) 156824, https://doi.org/10.1016/j.apsusc.2023.156824.

[30] Z.-J. Ding, Y.-P. Wang, W.-J. Liu, S.-J. Ding, M.R. Baklanov, D.W. Zhang, Characterization of PECVD ultralow dielectric constant porous SiOCH films using triethoxymethylsilane precursor and cinene porogen, J. Phys. D. Appl. Phys. 51 (2018) 115103, https://doi.org/10.1088/1361-6463/aaae79.

[31] Y.K. Sa, J. Bang, J. Son, D.-Y. Yu, Y.-C. Kim, Enhanced thermo–mechanical reliability of ultralow-k dielectrics with self-organized molecular pores, Materials 14 (2021) 2284, https://doi.org/10.3390/ma14092284.

[32] S. Kwon, W. Ban, H. Kim, Y. Park, Y. Kim, S. Yu, D. Jung, Single precursor based ultra-low k thin film deposited with tetrakis(trimethylsilyloxy)silane in PECVD system, Sci. Adv. Mater. 10 (2018) 1147–1153, https://doi.org/10.1166/sam.2018.3292.

[33] D. Priyadarshini, S.V. Nguyen, H. Shobha, E. Liniger, J.H.-C. Chen, H. Huang, S. A. Cohen, A. Grill, Advanced single precursor based pSiCOH k = 2.4 for ULSI interconnects, J. Vac. Sci. & Technol. B 35 (2017) 021201, https://doi.org/10.1116/1.4974317.

[34] H. Miyajima, H. Masuda, K. Watanabe, K. Ishikawa, M. Sekine, M. Hori, Chemical bonding structure in porous SiOC films (k < 2.4) with high plasma-induced damage resistance, Micro and Nano Eng. 3 (2019) 1–6, https://doi.org/10.1016/j.mne.2019.02.005.

[35] C. Kubasch, T. Olawumi, H. Ruelke, U. Mayer, J.W. Bartha, Investigation of argon plasma damage on ultra low-κ dielectrics, ECS J. Solid state, Sci. Technol. 4 (2015), https://doi.org/10.1149/2.0041501jss. N3023–N 3028.

[36] X. Guo, J.E. Jakes, S. Banna, Y. Nishi, J.L. Shohet, Effects of plasma and vacuum-ultraviolet exposure on the mechanical properties of low-k porous organosilicate glass, J. Appl. Phys. 116 (2014) 044103, https://doi.org/10.1063/1.4891501.

[37] M.R. Baklanov, V. Jousseaume, T.V. Rakhimova, D.V. Lopaev, Yu.A. Mankelevich, V.V. Afanas'ev, J.L. Shohet, S.W. King, E.T. Ryan, Impact of VUV photons on SiO2 and organosilicate low-k dielectrics: general behavior, practical applications, and atomic models, Appl. Phys. Rev. 6 (2019) 011301, https://doi.org/10.1063/1.5054304.

[38] N. Posseme, T. Chevolleau, O. Joubert, L. Vallier, P. Mangiagalli, Etching mechanisms of low-k SiOCH and selectivity to SiCH and SiO2 in fluorocarbon based plasmas, J. Vac. Sci. & Technol. B 21 (2003) 2432, https://doi.org/10.1116/1.1627337.

[39] Y. Afandi, G. Parish, A. Keating, Surface micromachining multilayer porous silicon for spectral filtering applications, Mater. Sci. Semicond. Process. 138 (2022) 106314, https://doi.org/10.1016/j.mssp.2021.106314.

[40] H.W. Tak, J.K. Jang, D. Sung, D.S. Kim, D.W. Kim, G.Y. Yeom, Etch characteristics of nanoscale ultra low-k dielectric using C3H2F6, Mater. Express 10 (2020) 834–840, https://doi.org/10.1166/mex.2020.1777.

[41] S. Lee, J. Woo, D. Jung, J. Yang, J. Boo, H. Kim, H. Chae, Effect of etching on dielectric constant and surface composition of SiCOH low-k films in inductively coupled fluorocarbon plasmas, Thin Solid Films 517 (2009) 3942–3946, https://doi.org/10.1016/j.tsf.2009.01.104.

[42] T.E.F.M. Standaert, M. Schaepkens, N.R. Rueger, P.G.M. Sebel, G.S. Oehrlein, J. M. Cook, High density fluorocarbon etching of silicon in an inductively coupled plasma: mechanism of etching through a thick steady state fluorocarbon layer, J. Vac. Sci. & Technol. A 16 (1998) 239–249, https://doi.org/10.1116/1.580978.

[43] Y.S. Tan, S.Y.M. Chooi, C.-Y. Sin, P.-Y. Ee, M.P. Srinivasan, S.O. Pehkonen, Characterization of low-k dielectric trench surface cleaning after a fluorocarbon etch, Thin Solid Films 462–463 (2004) 250–256, https://doi.org/10.1016/j.tsf.2004.05.053.

[44] S. Zimmermann, N. Ahner, F. Blaschta, M. Schaller, H. Zimmermann, H. Rülke, N. Lang, J. Röpcke, S.E. Schulz, T. Gessner, Influence of the additives argon, O2, C4F8, H2, N2 and CO on plasma conditions and process results during the etch of SiCOH in CF4 plasma, Microelectron. Eng. 88 (2011) 671–676, https://doi.org/10.1016/j.mee.2010.07.001.

[45] H. Jang, H. Kim, S. Lee, H. Moon, D. Jung, H. Chae, Characterization of low-k SiCOH film etching in fluorocarbon inductively coupled plasmas, Nanosci. Nanotechnol. Lett. 9 (2017) 174–178, https://doi.org/10.1166/nnl.2017.2332.

[46] N. Posseme, T. Chevolleau, O. Joubert, L. Vallier, N. Rochat, Etching of porous SiOCH materials in fluorocarbon-based plasmas, J. Vac. Sci. & Technol. B 22 (2004) 2772, https://doi.org/10.1116/1.1815316.

[47] W. Wirth, J. Comeaux, S. Jang, Characterization of flexible low-dielectric constant carbon-doped oxide (SiCOH) thin films under repeated mechanical bending stress, J. Mater. Sci. 57 (2022) 21411–21431, https://doi.org/10.1007/s10853-022-07987-y.

[48] A.M. Efremov, D.B. Murin, K.-H. Kwon, Concerning the effect of type of fluorocarbon gas on the output characteristics of the reactive-ion etching process, Russ. Microelectron. 49 (2020) 157–165, https://doi.org/10.1134/S1063739720020031.

[49] I. Chun, A. Efremov, G.Y. Yeom, K.-H. Kwon, A comparative study of CF4/O2/Ar and C4F8/O2/Ar plasmas for dry etching applications, Thin Solid Films 579 (2015) 136–143, https://doi.org/10.1016/j.tsf.2015.02.060.

[50] C. Cardinaud, Fluorine-based plasmas: Main features and application in micro-and nanotechnology and in surface treatment, C. R. Chimie 21 (2018) 723–729, https://doi.org/10.1016/j.crci.2018.01.009.

[51] M.R. Baklanov, J.-F. de Marneffe, D. Shamiryan, A.M. Urbanowicz, H. Shi, T. V. Rakhimova, H. Huang, P.S. Ho, Plasma processing of low-k dielectrics, J. Appl. Phys. 113 (2013) 041101, https://doi.org/10.1063/1.4765297.

[52] K. Lionti, W. Volksen, T. Magbitang, M. Darnon, G. Dubois, Toward successful integration of porous low-k materials: strategies addressing plasma damage, ECS J. Solid State Sci. Technol. 4 (2015) N3071–N3083. https://doi.org/https://doi.org/10.1149/2.0081501jss.

[53] Y. Sun, M. Krishtab, H. Struyf, P. Verdonck, S. De Feyter, M.R. Baklanov, S. Armini, Impact of plasma pretreatment and pore size on the sealing of ultralow-k dielectrics by self-assembled monolayers, Langmuir 30 (2014) 3832–3844, https://doi.org/10.1021/la404165n.

[54] C.J. Mogab, A.C. Adams, D.L. Flamm, Plasma etching of Si and SiO2 -the effect of oxygen additions to CF 4 plasmas, J. Appl. Phys. 49 (1978) 3796–3803, https://doi.org/10.1063/1.325382.
[55] J.H. Choi, J. Yoon, Y. Jung, K.W. Min, W.B. Im, H.-J. Kim, Analysis of plasma etching resistance for commercial quartz glasses used in semiconductor apparatus in fluorocarbon plasma, Mater. Chem. Phys. 272 (2021) 125015, https://doi.org/10.1016/j.matchemphys.2021.125015.
[56] E. Kunnen, M.R. Baklanov, A. Franquet, D. Shamiryan, T.V. Rakhimova, A. M. Urbanowicz, H. Struyf, W. Boullart, Effect of energetic ions on plasma damage of porous SiCOH low-k materials, J. Vac. Sci. & Technol. B 28 (2010) 450–459, https://doi.org/10.1116/1.3372838.
[57] S.-K. Kwak, K.-H. Jeong, S.-W. Rhee, Nanocomposite low-k SiCOH films by direct PECVD using vinyltrimethylsilane, J. Electrochem. Soc. 151 (2004) F11–F16, https://doi.org/10.1149/1.1636738.
[58] C.-H. Lo, M.-H. Lin, K.-S. Liao, M. De Guzman, H.-A. Tsai, V. Rouessac, T.-C. Wei, K.-R. Lee, J.-Y. Lai, Control of pore structure and characterization of plasma-polymerized SiOCH films deposited from octamethylcyclotetrasiloxane (OMCTS), J. Membr. Sci. 365 (2010) 418–425, https://doi.org/10.1016/j.memsci.2010.09.042.
[59] J. Bao, H. Shi, J. Liu, H. Huang, P.S. Ho, M.D. Goodner, M. Moinpour, G.M. Kloster, Mechanistic study of plasma damage of low k dielectric surfaces, J. Vac. Sci. & Technol. B 26 (2008) 219–226, https://doi.org/10.1116/1.2834562.
[60] A. Brady-Boyd, R. O'Connor, S. Armini, V. Selvaraju, M. Pasquali, G. Hughes, J. Bogan, The role of atomic oxygen in the decomposition of self-assembled monolayers during area-selective atomic layer deposition, Appl. Surf. Sci. 586 (2022) 152679, https://doi.org/10.1016/j.apsusc.2022.152679.
[61] J. Comeaux, W. Wirth, J. Courville, N.-W. Baek, D. Jung, S. Jang, Etching characteristics of low-k SiCOH thin films under fluorocarbon-based plasmas, Vacuum 202 (2022) 111165.
[62] Y. Lin, T.Y. Tsui, J.J. Vlassak, Octamethylcyclotetrasiloxane-based, low-permittivity organosilicate coatings: composition, structure, and polarizability, J. Electrochem. Soc. 153 (2006) F144–F152, https://doi.org/10.1149/1.2202120.
[63] C.Y. Kim, A.S. Jung, R. Navamathavan, C.K. Choi, Bonding configuration and electrical properties of carbon-incorporated low-dielectric-constant SiOC(-H) films with nano-pore structures deposited by using PECVD, J. Korean Phys. Soc. 53 (2008) 2621–2626, https://doi.org/10.3938/jkps.53.2621.
[64] J.F. Moulder, W.F. Stickle, P.E. Sobol, K.D. Bomben, Handbook of X-Ray Photoelectron Spectroscopy, second ed., Perkin-Elmer Corporation, Minnesota, 1992.
[65] P. Wang, Q. Cheng, C. Mao, W. Su, L. Yang, G. Wang, L. Zou, Y. Shi, C. Yan, Z. Zou, H. Yang, Regulation of oxygen vacancy within oxide pyrochlores by F-doping to boost oxygen-evolution activity, J. Power Sources 502 (2021) 229903, https://doi.org/10.1016/j.jpowsour.2021.229903.
[66] O.V. Braginsky, A.S. Kovalev, D.V. Lopaev, E.M. Malykhin, A. Mankelevich Yu, T. V. Rakhimova, A.T. Rakhimov, A.N. Vasilieva, S.M. Zyryanov, M.R. Baklanov, The mechanism of low-k SiOCH film modification by oxygen atoms, J. Appl. Phys. 108 (2010) 073303, https://doi.org/10.1063/1.3486084.